

Undergraduate Honors Thesis

Measuring the Hall Effect in Dopings of $\text{Mn}_3\text{Si}_2\text{Te}_6$

By: **Alexander Fix**

Advisor: **Professor Gang Cao** (Physics)

Honors Council Representative: **Professor Paul Beale** (Physics)

Outside Reader: **Professor David Malaspina**

(Astrophysical and Planetary Sciences)

Physics Department, College of Arts and Sciences

University of Colorado at Boulder

March 22nd, 2024

ABSTRACT

Colossal Magnetoresistance (CMR) is an ill-understood property of some materials wherein resistance is reduced by several orders of magnitude when a magnetic field is applied. This is an even more extreme version of the well-known Giant Magnetoresistance (GMR) that finds applications in numerous memory storage devices today, meaning better understanding of CMR or knowledge of more CMR materials could prove highly beneficial. $\text{Mn}_3\text{Si}_2\text{Te}_6$ is one such material, exhibiting a strong and unusual CMR effect when a magnetic field is applied along the c-axis. The MnTe structures within the crystal are believed to be responsible, so this study dopes other metals in for the Mn to observe the effect on electrical transport with a similar structure and less Mn. Cu and In were successfully doped in at concentrations of 15% and 30%. The Hall Effect was then measured in the doped samples, and from this the charge carrier densities determined and compared to the original undoped material. It was found that 15% dopings preserve a diminished form of $\text{Mn}_3\text{Si}_2\text{Te}_6$'s properties while introducing new behavior related to the dopant ion, but 30% dopings induce more erratic behavior.

ACKNOWLEDGEMENTS

I extend the deepest gratitude to the other members of my research group for their support in this project. In particular, my advisor Professor Gang Cao taught me about $\text{Mn}_3\text{Si}_2\text{Te}_6$ and its interesting properties. Dr. Yifei Ni spent countless hours teaching me every step of crystal synthesis as well as passing on his advice for synthesizing pure and doped MST. Yu Zhang gave me detailed instruction on the use of various measurement devices for characterizing the samples as well as discussing the theory of the Anomalous Hall Effect and how I could properly fit for it. Anish Parulekar provided valuable insight in how to ensure my methods were rigorous, data well-processed, and results properly presented.

Outside of my research group, the wonderful professors in the Physics Department at CU Boulder encouraged me to begin work on this thesis process and provided me with the experimental and theoretical backgrounds necessary for such an undertaking. Finally, but perhaps most importantly, I also received valuable support, thesis feedback, and genuine friendship from my fellow students Calder Haubrich, Noah Welikson, Giorgio Matessi, Matt Guerrero, Graham Mauer, Luke Coffman, Sean Gopalakrishnan, Andy Hicks, Isaac Alhusseini, Sierra Genne, Eleanor Gentry, Sam Campau, and Nick Entin.

Table of Contents

Abstract	i
Acknowledgments	ii
Chapter 1: Introduction	1
1.1 Thesis Outline	1
1.2 Colossal Magnetoresistance	1
1.3 $\text{Mn}_3\text{Si}_2\text{Te}_6$	2
Chapter 2: Background	4
2.1 Doped Compounds	4
2.2 The Hall Effect	5
2.3 The Anomalous Hall Effect	6
Chapter 3: Methods	8
3.1 Crystal Synthesis	8
3.2 Checking Crystal Composition	11
3.3 Measuring Resistivity (Hall and Longitudinal)	12
3.4 Measuring Magnetization	15

3.5	Fitting for Anomalous Hall Effect and Determining Carrier Density	16
Chapter 4: Results		18
4.1	Cu-Doped $\text{Mn}_3\text{Si}_2\text{Te}_6$	19
4.1.1	15% Cu	19
4.1.2	30% Cu	21
4.2	In-Doped $\text{Mn}_3\text{Si}_2\text{Te}_6$	23
4.2.1	15% In	23
4.2.2	30% In	25
4.2.3	In-Doped Magnetization vs. Temperature	27
Chapter 5: Discussion		28
Chapter 6: Conclusion		33
References		36

Chapter 1

Introduction

1.1 Thesis Outline

This thesis details methods for doping $\text{Mn}_3\text{Si}_2\text{Te}_6$ single crystals with varying amounts of In and Cu, measurements of the Hall Effect and various physical properties to estimate the charge carrier densities in these doped compounds, and a discussion of how these carrier densities compare to each other and the base compound to reveal more information about electrical transport in $\text{Mn}_3\text{Si}_2\text{Te}_6$.

First, to motivate this research, the following "Introduction" sections shall introduce the concept of colossal magnetoresistance and the unique way it manifests in $\text{Mn}_3\text{Si}_2\text{Te}_6$ that make this compound important to study. Further supporting information will then be discussed in the "Background" sections to explain the process of doping, the choice of dopants, and how the Hall Effect can be used to determine charge carrier density. With the necessary prerequisites covered, the "Methods" section will detail all the experimental procedures from initial crystal synthesis to finally fitting Hall Effect data. The "Results" section will then display the products of this data collection and analysis, the significance of which is covered in "Discussion", before the final "Conclusion" summarizes the work and looks toward avenues for further study in the future.

1.2 Colossal Magnetoresistance

Magnetoresistance refers broadly to any effect in a material where the value of its electrical resistance changes in response to an external magnetic field, though the change is typically only a few

percent [1]. Ordinary magnetoresistance was first discovered in 1856 by William Thomson (better known as Lord Kelvin), and has become very well known and studied in the century and a half since then [2]. More recently, in 1988 giant magnetoresistance (GMR) was discovered by both Albert Fert and Peter Grunberg (winning them the 2007 Nobel Prize in Physics) [3]. Giant magnetoresistance arises in multilayer materials that alternate ferromagnetic and non-magnetic layers and exhibit very high resistance when a magnetic field is oriented along one direction and very low when it's oriented along another, leading to a resistance drop between the high and low states of 50% or more [3]. This much larger effect compared to ordinary types of magnetoresistance makes GMR useful for a variety of applications, particularly the magnetic memory storage now used in most modern computers, as this extreme sensitivity to magnetic field can be used to read off binary data encoded in varying magnetic alignments in the storage material [3].

An even more extreme example of magnetoresistance is colossal magnetoresistance (CMR), which can cause a resistance decrease of several orders of magnitude in a material [4]. Unlike GMR which occurs in multilayer materials, CMR occurs in single materials (typically Mn-based perovskite oxides) and appears to be tied to a phase transition from ferromagnetism to paramagnetism [4]. At present there is far less theoretical understanding of CMR than other types of magnetoresistance, and most materials that manifest CMR only do so at a low transition temperature, making CMR far less practical than GMR for technological applications. However, this makes the study of CMR materials all the more important, as greater understanding could make the effect easier to manifest and control, further expanding the technological progress allowed by GMR technology.

1.3 $\text{Mn}_3\text{Si}_2\text{Te}_6$

One material that manifests colossal magnetoresistance is $\text{Mn}_3\text{Si}_2\text{Te}_6$ [5]. This material exhibits a seven-order of magnitude reduction in resistivity when a magnetic field is applied below a transition temperature T_C of 78 K, but interestingly this CMR only occurs when the magnetic field

is applied along the c axis [6]. In other materials CMR occurs when the magnetic field is applied along the ab plane, polarizing the spins in one direction so charge can flow easily without charge carriers being scattered [6]. A proposed explanation for the odd behavior in $\text{Mn}_3\text{Si}_2\text{Te}_6$ is the presence of chiral orbital currents (COC) that flow around the edges of the MnTe octohedra in the crystal below T_C [5]. Ordinarily they would flow in random directions, cancelling to no net current and having no impact, but an external magnetic field along the c -axis would align with the magnetic moments of the currents, strengthening them along one direction to reduce scattering and allow better charge flow (and hence a dramatic reduction in resistance) [5]. It is clear then that $\text{Mn}_3\text{Si}_2\text{Te}_6$ displays an unconventional type of CMR, so further study of this compound and how charge can flow through it may reveal new understanding of the CMR effect. With this context of CMR and how it arises in $\text{Mn}_3\text{Si}_2\text{Te}_6$, this study is then motivated: doping other elements in for Mn and measuring charge carrier density to gain a deeper understanding of CMR.

Chapter 2

Background

2.1 Doped Compounds

In the context of Condensed Matter Physics, doping refers to the intentional introduction of impurities into a material to alter its electrical, optical and/or structural properties [7]. Arguably the most famous and important example of this is the doping of elements that add mobile charge carriers into semiconductors such as Si and GaAs, increasing their conductivity [7]. There are many ways to dope a material, but the method used in this work is the simple addition of dopant elements during synthesis of the crystalline compounds. In this case, the dopant element has similar atomic properties (atomic radius, valence electrons, etc.) to the element it's replacing, and when mixed in during synthesis will substitute for the original element in the final crystalline lattice, producing a relatively uniform concentration of doping in the crystals [8].

For this study, dopings were synthesized to replace Mn with other elements in order to investigate the impact it plays on CMR in $\text{Mn}_3\text{Si}_2\text{Te}_6$. To this end, two other elements were selected as dopants - the 3d transition metal Cu and the 4d other metal In. Both have similar atomic radii to Mn, allowing them to dope well [9]. Cu is in fact very similar to Mn, also being a transition metal and manifesting in an oxidation state of +2, so doping it in for Mn will reveal whether Mn specifically causes the observed behavior or if any transition metal will work (or perhaps be better) [10]. On the other hand, In is notably different being a non-transition metal and a diamagnetic materials (where Mn and Cu (II) are paramagnetic), so its presence will demonstrate the impacts the inherent magnetic state of the ions have on enhancing or disrupting CMR [10].

2.2 The Hall Effect

The Hall Effect, first discovered by Edwin Hall in 1879, is a phenomenon where when current is run one direction through a conductor and an external magnetic field applied normal to the current, an additional voltage is induced normal to both the applied current and magnetic field [11]. This is due to the Lorentz force causing charge carriers to drift in the transverse direction to one side of the material, leading to a charge buildup and resultant transverse voltage difference [12]. As the charge builds up an electric field is induced by the voltage difference, and the system reaches an equilibrium where the force from this electric field balances out the force from the applied magnetic field, giving a fixed Hall Voltage V_H at a given set of conditions [12]. A diagram of this can be seen below in Figure 2.1.

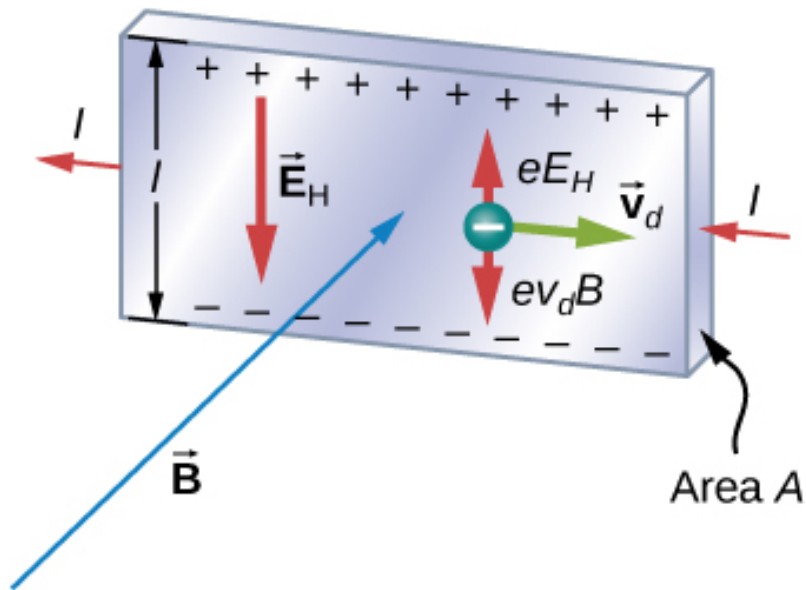


Figure 2.1: Diagram of the Hall Effect influencing the movement of electrons in a material. [12]

With this background, an expression can be derived for the Hall Voltage, and in turn the Hall Resistivity can be found in terms of charge carrier density.

The Lorentz Force is given by $\vec{F} = q(\vec{E} + \vec{v} \times \vec{B})$. As described, the net force in this scenario is 0 (this is a steady state), so then $0 = e(E - v_d B) \rightarrow E = v_d B$ where v_d is the drift velocity of the

charge carriers and e is the elementary charge. This then implies $v_d = \frac{E}{B}$.

Simultaneously, the current flowing across the material can be expressed in terms of the drift velocity as $I = nev_dA$ where n is the charge carrier density and A the cross-sectional area of the material. Substituting for v_d , $I = ne\left(\frac{E}{B}\right)A$.

By the definition of electric field, $E = \frac{V_H}{l}$ where V_H is the Hall Voltage and l is the distance between the sides of the material, across which this voltage difference occurs.

$$I = ne\left(\frac{V_H}{Bl}\right)A \rightarrow V_H = \frac{IBl}{neA}$$

Resistivity is defined as $\rho = \frac{RA}{l} = \frac{VA}{Il}$.

$$\text{Then the Hall Resistivity } \rho_H = \rho_{xy} = \frac{V_H A}{Il} = \frac{B}{ne}$$

This reveals that under the ordinary Hall Effect, the Hall resistivity is linearly proportional to applied magnetic field, and the coefficient of this proportionality is $\frac{1}{ne}$, often labelled the Hall Coefficient R_H [13]. The Hall Coefficient will be the slope of the line r_{xy} vs. B , so by measuring the Hall Resistivity over a varying magnetic field, the charge carrier density can then be determined. This allows a microscopic property of materials that affects electrical transport to be measured when it couldn't by other means [13].

2.3 The Anomalous Hall Effect

While ordinarily the Hall Effect leads to a linear resistivity vs applied field, making calculation of charge carrier density straightforward, many materials additionally exhibit a group of phenomena known as the Anomalous Hall Effect (AHE) [14]. At lower magnetic fields, the AHE induces a far larger voltage (and thus resistivity) [14]. There is no one cause for the AHE, and the theoretical mechanisms are still being debated [14]. Nevertheless, enough is known to functionally describe the portion of Hall resistivity from the AHE. Materials manifesting Anomalous Hall may contain a term in resistivity proportional to $\rho_{xx}(H)M(H)$ for skew-scattering of charge carriers, a term proportional to $\rho_{xx}^2(H)M(H)$ for intrinsic or side-jump impacts, or both, where ρ_{xx} is longitudinal resistivity, M is magnetization, and H is applied magnetic field [14]. Thus the overall expression

for Hall resistivity is $\rho_{xy}(H) = R_H H + A\rho_{xx}(H)M(H) + B\rho_{xx}^2(H)M(H)$ where A and B are constants [14].

$\text{Mn}_3\text{Si}_2\text{Te}_6$ is a material that manifests AHE at lower temperatures, so while the charge carrier density can still be calculated from the ordinary Hall Effect, the contribution to ρ_{xy} from anomalous effects must first be determined and subtracted out. To accomplish this, in addition to Hall Resistivity, longitudinal resistivity and magnetization were measured for the samples in this study and the anomalous effect fitted and removed from Hall Resistivity, the details of which are discussed in Sections 3.3-3.5.

Chapter 3

Methods

3.1 Crystal Synthesis

Single crystals of $\text{Mn}_3\text{Si}_2\text{Te}_6$, doped with varying amounts of Cu and In in place of Mn, were synthesized using a flux method. First, open-ended silica quartz ampoules were prepared by cutting a hollow silica quartz tube into 40 cm segments and sealing and separating the rods in the middle with a Hydrogen-Oxygen flame to create pairs of 20 cm ampoules. Small indentations were also made in the ampoules with the flame for sealing the compounds later.

For chalcogenide samples such as these, Oxygen contamination from the atmosphere is a serious risk as Oxygen belongs to the same group as Chalcogens like Tellurium and can easily bond to the other elements, ruining the samples. Therefore, the ampoules were transferred to an Ar-filled glovebox for sample preparation. Within the glovebox are stored 3-5N quality pure elements, also packed under Argon, which were used for the samples. 2g total of Mn, Si, and Te were measured into each ampoule in stoichiometric amounts for $\text{Mn}_3\text{Si}_2\text{Te}_6$ as a base. An additional 1g of Te and .1g of Si were added to each to act as a flux for crystal growth. For each doping, an amount of the dopant was then added that would be equivalent to X% of $\text{Dopant}_3\text{Si}_2\text{Te}_6$. For example, 2g of stoichiometric $\text{Cu}_3\text{Si}_2\text{Te}_6$ would contain around .377g Cu, so the 15% Cu samples were prepared by adding $.15 * .377 \text{ g} = .075 \text{ g}$ Cu to the base mixture for pure $\text{Mn}_3\text{Si}_2\text{Te}_6$. Finally, a small quantity of quartz wool was placed above the elements in the ampoules for later use in separating the grown crystals from the flux.

Before removing the samples from the glovebox, 1.5 cm segments were cut from a solid silica

quartz rod and squares of parafilm were cut from a larger sheet to prepare for sealing the samples. After the ampoules were removed from the glovebox, one of the glass rod pieces was swiftly placed inside (resting on the indentations made earlier) and the open ends of the ampoules sealed with a wrapping of parafilm to minimize atmospheric exposure until they could be sealed.

To seal each ampoule, the parafilm was removed and the ampoule connected to a pressure valve and vacuum pump. The vacuum pump was used to steadily remove gas from the ampoules down to a pressure of 50 milliTorr before the pressure valve was closed and the pump disconnected. Keeping the pressure valve on to maintain this near-vacuum, a Hydrogen-Oxygen flame was lit and carefully applied to the region of the ampoule where the glass rod pieces had been placed atop the indentation. This serves to melt the wall of the ampoule onto the solid glass rod, sealing in the measured elements. The pressure valve is then released and the top of the ampoule sealed by melting in another section above the glass rod point, providing an additional buffer. For reference, photographs of ampoules during and after flame sealing are included in Figure 3.1.



Figure 3.1: Left: An in-progress photo of an ampoule being sealed. Shortly before this photo, a vacuum pump (not pictured) and the vacuum gauge were used to reduce pressure to near-vacuum. The Hydrogen-Oxygen flame on the right is used for sealing the ampoules. Right: Ampoules of Cu and In doped $\text{Mn}_3\text{Si}_2\text{Te}_6$ after being sealed.

Once the ampoules are sealed, the samples are ready to be heated in a furnace so actual crystal growth can occur. All ampoules for this study were baked in a KSL 1200-X furnace using the

following sequence:

Heat from room temperature to 1150°C over 12 hours, hold the temperature at 1150°C for 30h, cool at a steady rate to 550°C over 10 days.

It's possible that future testing of this recipe may reveal quality crystals can be grown in a shorter time, but earlier testing found a cooling time of only 5 days insufficient to produce crystals with length > 1 mm, which makes it difficult to perform measurements on the final samples.

At this point, the samples can be allowed to cool to room temperature as sizeable crystals of the desired composition will be present in the ampoules. However, doing so also allows the Te flux to cool and solidify around the crystals, making extraction of the crystals for measurement a more difficult and lengthy process. Instead, the furnace is held at 550°C once cooling is complete and the ampoules are swiftly removed and placed upside down (so that the sample mixture lies above the quartz wool) in an Eppendorf Centrifuge 5702. Before the samples have time to cool to below 450°C (the melting point of Te), the centrifuge is run at 4400 RPM for 3 minutes. The purpose of this is that while the flux is still liquid, it can permeate through the quartz wool while any large crystals remain behind, and the swift rotation of the centrifuge augments this process and serves to shake flux from the crystals. The flux then swiftly solidifies as it cools, leaving it unable to pass back through the wool so the crystals can be isolated more easily.

With single crystals synthesized, the ampoules are then placed in a vent hood and mechanically broken. The venting does not aid in preserving the crystals, but chalcogenide samples can release a pungent odor, so placing them under a vent hood for a few minutes before sealing them away is recommended. The contents of the broken ampoules are then examined and any potential crystals are isolated with tweezers and sealed away until such time as their composition can be confirmed, details on which are contained in the next section.

3.2 Checking Crystal Composition

Once quality single crystals were grown, their compositions were confirmed with Energy-Dispersive X-ray Spectroscopy (EDX, sometimes called EDS) [15]. EDX functions by using an X-ray or electron beam to strike the surface of the crystals to be measured, exciting the atoms within them. The excited atoms then emit X-rays, which are picked up by an X-ray detector and analyzed. As all atoms have distinct wavelengths of emission based on their atomic structure and electron orbital filling, the patterns of X-rays detected can be used to determine whether a specific element is present, and the amount of one set of X-rays relative to another indicates the relative abundance of elements [15].

These EDX measurements were performed using a Hitachi TM3030Plus Scanning Electron Microscope (SEM) paired with an Oxford Instruments EDX spectrometer and x-stream data analysis computer. To use the SEM, samples were selected from each batch of crystals with relatively smooth, even faces for easy spectroscopy. The samples were then affixed to a measurement stub designed for the instrument with double-sided conducting tape. An example of this can be seen in Figure 3.2. The height of the stub is adjusted so the tops of the samples will be roughly 8.5 mm from the EDX spectrometer using a specimen height setting tool paired with the instruments [15]. A diagram is shown in Figure 3.2. Once the samples are on the stub and set to the correct height, the SEM chamber is brought to atmospheric pressure and opened, the samples inserted, and then the chamber evacuated to allow the SEM to function without exciting large amounts of atmospheric gasses.

With everything configured, the actual images of the samples and EDX spectra are taken using the included Hitachi TM3030Plus software and Oxford Instruments' AZtec One. The Hitachi software displays an image of the current field of view of the SEM and allows for zooming in and out as well as focusing, allowing the desired samples to be identified and imaged [15]. The AZtec One software is able to link to the Hitachi, so an electron image can be captured for each sample [16]. While the SEM is still focused in this position, an area can be selected on this image for the

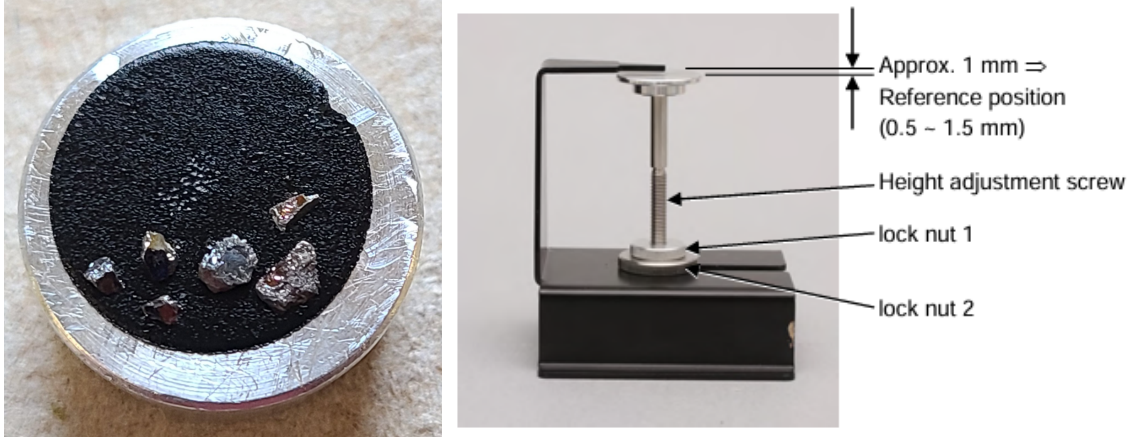


Figure 3.2: Left: A measurement puck used for holding crystals during SEM analysis and EDX measurements.

Right: A diagram of the height setting tool used for EDX measurements [15].

EDX spectrometer to capture spectra.

During and after the data collection, the weight percentage abundances of each element will be displayed and can be set to automatically convert to atomic % (% of moles present) which can be used to confirm composition [16]. For example, a sample could be suggested to be pure $\text{Mn}_3\text{Si}_2\text{Te}_6$ if the percentages are roughly $\frac{3}{11}$ for Mn, $\frac{2}{11}$ for Si, and $\frac{6}{11}$ for Te (as these are the molar ratios). One could then determine a doping percentage by seeing how the dopant and element it's replacing compare to the percentage in a pure sample (i.e., for 15% Cu, there would be $.15 * \frac{3}{11}$ Cu and $.85 * \frac{3}{11}$ Mn as Cu replaces Mn). It should be noted that this doesn't guarantee composition, as dust or a layer of one set of elements may reside on the surface of the sample, but to mitigate this risk samples are only used for measurement if they appear clean, and if a sample were radically different than expected (i.e. actually undoped when it appears to be doped due to a dirty surface), this would become apparent when measuring bulk properties and lead to a reinvestigation of composition.

3.3 Measuring Resistivity (Hall and Longitudinal)

Actual measurements of the Hall effect were carried out with the Quantum Design DynaCool Physical Property Measurement System (PPMS). This system can achieve temperatures as low as 2 K using a liquid He pump and magnetic fields as high as 14 T using a superconducting solenoid,

making it ideal for characterizing the samples over a wide range of extreme conditions [17]. A variety of measurement devices can be inserted into the PPMS to measure different properties. Both the Hall (transverse) and longitudinal resistances of a sample can be measured with the Electrical Transport Option (ETO) module by mounting the samples onto a puck and wiring them to electrodes to run current and measure voltage in different ways [18].

For all resistance measurements, a 4-wire system is employed. While resistance can be measured with only two points of electrical contact, when measuring low-resistance samples, the contact resistance at these points can be measurably high, disrupting the results [19]. To circumvent this, two electrical contacts supply the current while two more are used to measure the voltage drop across a distance (from which resistance can be inferred), as this way they act in series with the current flow along the sample and don't add significant additional resistance [19]. To further reduce added resistance, all the electrical contacts on the crystals are thin ($\approx 25\mu\text{m}$ diameter) gold wires as gold is highly conducting. The gold wires are affixed to the samples with a silver epoxy (also highly conducting) and then baked at a temperature of around $300\text{ }^\circ\text{C}$ to solidify the epoxy and bond the wires to the sample.

Different wire configurations are ordinarily used for measuring the two directions of resistivity. To measure Hall resistivity, as the voltage difference is induced normal to both applied magnetic field and current, the current leads are placed on two sides of a sample and the voltage leads across from each other on the same plane. For longitudinal resistivity, both voltage leads are placed in line with each other between the current leads. However, in this instance since both needed to be measured, a hybrid configuration was used with two sets of voltage leads across from each other so both types of resistance could be measured without changing the contacts. This also provides backups so the pair of leads with lower contact resistance could be selected. Diagrams of all three of these potential configurations are shown in Figure 3.3.

Once leads were attached to a set of crystals to be measured, they were affixed to a PPMS ETO measurement puck with varnish. The pucks all contain 12 exposed electrodes split into 3 channels of 4 electrodes, so the gold wires were then wound around these electrodes and a coat of silver

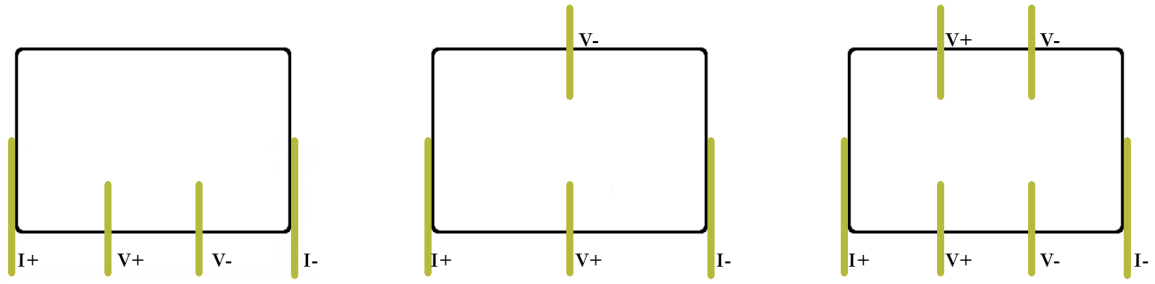


Figure 3.3: Left: Configuration of leads on a crystal for measuring longitudinal resistivity. Center: Configuration of leads on a crystal for measuring Hall resistivity. Right: Configuration of leads on a crystal for measuring both simultaneously. The V+ and V- leads pair together for Hall, and this method provides redundant measurement pairs in case one wire has poor contact.

paint applied to establish strong contacts. Four leads for longitudinal resistivity were attached to the electrodes on channels 1 and 2, and channel 3 was used for additional voltage leads for Hall, as shown in Figure 3.4. Before making the measurements, the contact resistance was tested by inserting the puck into a measurement station with outputs tied to the 12 electrodes, allowing the resistance between them to be measured with a standard multi-meter. All contacts used were established to have a resistance of $5\text{ k}\Omega$ or less before measurement.

Once the contacts are confirmed to be strong, the measurement puck can be inserted into the PPMS and various parameters adjusted and measurements taken with its built-in software. Once ETO measurement is enabled, the PPMS can run a set current between the current leads and measure the voltage difference between the voltage leads, which is then output as a resistance value in Ω using Ohm's Law: $V = IR \rightarrow R = \frac{V}{I}$ [18]. With the 4-lead measurement, current draw from the voltage leads is significantly low enough for this resistance value to be accurate [18]. Both Hall and longitudinal resistance are measured this way by adjusting which of the leads are measured as the voltage leads. Using this method, datasets were collected for a sweep of applied c-axis magnetic field from -14 T to 14T at multiple temperatures from 15 K to 200 K. Resistance is based on the exact conditions of the measurement, but use this data universally after measurement all resistances were converted to resistivity using the relation $\rho = \frac{RA}{l}$ where A is the cross sectional area of the sample and l is the distance between the voltage leads [18].

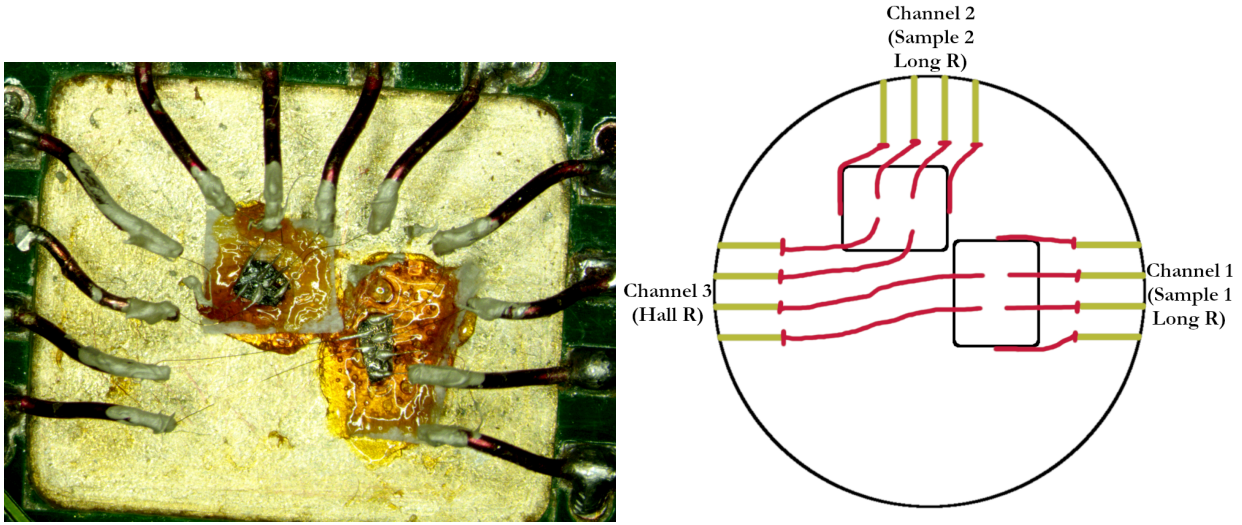


Figure 3.4: Left: 30% In and Cu doped $\text{Mn}_3\text{Si}_2\text{Te}_6$ samples mounted on the PPMS ETO puck for measurement.

Right: Schematic diagram of the samples on the puck, showing the 3 channels of electrodes and how the wires connect the crystals and electrodes for measuring electrical transport.

3.4 Measuring Magnetization

Magnetization for the samples was also measured in the PPMS using the Vibrating Sample Magnetometer (VSM) option. To carry out this measurement, samples were affixed to sapphire rods with varnish and the varnish allowed to dry overnight to provide a tight bond. Before taking the measurements, pickup coils were installed at the bottom of the PPMS chamber and a motor on top, linked by a tube to hold the sample and provide thermal insulation. Each sample on its rod was inserted into this apparatus and centered in the coils.

With this setup, the magnetic moment could be measured for each sample under different conditions. A time-dependent voltage will be induced in the coils given by $V_{\text{coil}} = \frac{d\phi}{dt} = \left(\frac{d\phi}{dz}\right)\left(\frac{dz}{dt}\right)$ where ϕ is magnetic flux through the coils, z the vertical position of the sample relative to the center of the coils, and t time [20]. The motor oscillates the vertical position of the rod holding a sample in a sinusoidal fashion, giving a voltage of $V_{\text{coil}} = 2\pi f C m A \sin(2\pi f t)$ where C is a coupling constant, m is the magnetic moment of the sample, A is the amplitude of oscillation, and

f is the frequency of oscillation [20]. In this way, the PPMS oscillates the samples and measures the voltages in the coil to determine magnetic moment. A schematic diagram of the entire process can be seen in Figure 3.5. Magnetic moment was measured for a -14 T to 14 T c-axis magnetic field sweep at the same temperatures as the resistivities.

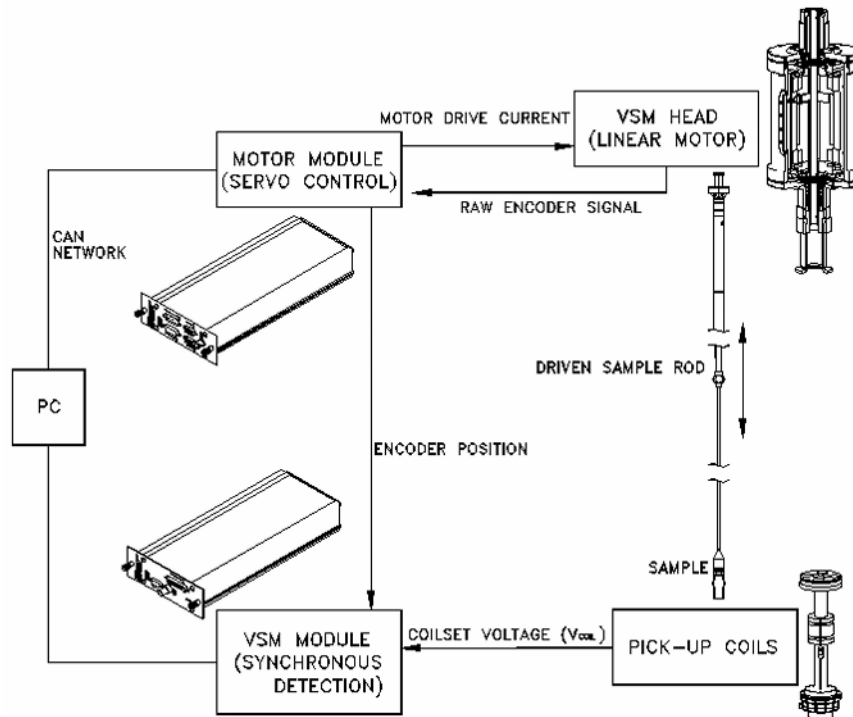


Figure 3.5: Schematic diagram of how the PPMS VSM option functions. [20]

3.5 Fitting for Anomalous Hall Effect and Determining Carrier Density

Once all data was acquired, it was able to be processed to achieve the desired result of carrier density information. The measured voltage, V_{meas} (and thus resistance) for the Hall Effect contains a combination of longitudinal and Hall voltages as it's impossible to perfectly align the Hall voltage leads. However, longitudinal voltage will have the same sign regardless of the direction of the magnetic field applied, so since data is collected over a field sweep from -14T to +14T, the Hall

Voltage V_{xy} can still be extracted from the data as

$$V_{xy}(H) = \frac{1}{2}[V_{\text{meas}}(H) - V_{\text{meas}}(-H)].$$

In this field sweep, some hysteresis is observed in the measurements. Hysteresis is when a physical property responds with a delay compared to the condition being changed, which causes a misalignment between the data when decreasing vs. increasing magnetic field. This is solved for splitting up the data as increasing and decreasing field portions of the sweep and only computing V_{xy} along one of those portions. This has been shown in other studies to consistently give the true behavior of V_{xy} independent of hysteresis [21].

Once Hall Voltage was extracted and converted back to resistance via $V = IR$, both the Hall and longitudinal resistances were converted to resistivity using $\rho = \frac{RA}{l}$, with A and l being measured from photographs of the samples. These resistances as well as the magnetization data were all imported into the Origin Pro software for processing.

Within Origin, a custom fitting function "Anomalous Hall" was defined to remove the Anomalous Hall Effect from the Hall Resistivity data. Matching the theoretical discussion of the AHE in Section 2.3, this fit was defined as: $\rho_{xy,AHE}(H) = A\rho_{xx}(H)M(H) + B\rho_{xx}^2(H)M(H)$. The datasets for ρ_{xy} , ρ_{xx} , and M were interpolated over a field range from -14 T to 14T at .1 T increments to ensure that the datapoints lined up at the same field values for fitting. The fit was then applied to each dataset that manifested the AHE, and the resulting fitted curve subtracted from the ρ_{xy} data to leave a close approximation of the contribution from the ordinary Hall Effect, especially at high magnetic field where the AHE is weaker. Fits were run until they converged with a χ_0 value of $\leq 10^{-9}$, indicating a very strong fit.

With only ordinary Hall remaining, the slope of that data was able to be used to determine charge carrier density. A linear regression fitting was run on each dataset from the range of 9 - 14 T, as the high field regime displays the cleanest linear behavior ensuring more consistent and accurate results, as discussed in other studies of this sample ([5], [6], [21]). The slope from these regressions is the Hall Coefficient, R_H , so charge carrier density was then determined from the slopes as $n = \frac{1}{R_H e}$.

Chapter 4

Results

Following are results from all of the samples measured. All results are shown from measuring properties while running 1mA of current through the samples. Data was also taken with 0.1mA, but this data is noisier while demonstrating similar trends, making its inclusion unnecessary.

The overall Hall Effect is shown for each sample from 0 - 14T at various temperatures (the negative field data is equal magnitude and asymmetric so for easier viewing of trends it's excluded from the plots) as well as the magnetization, ordinary Hall Effect after fitting, and charge carrier density.

As a final note before presenting results, the In-doped data is less complete than the Cu-doped due to it being more insulating. The measurement instruments used have a maximum compliance voltage of 105V which they cannot exceed lest the instruments be damaged. As a result, at lower temperatures and fields where resistance is higher the resistance could not be accurately measured on the In-doped samples within the voltage constraints. This can be seen on the plots by some Hall resistance datasets not extending fully from 0-14T.

4.1 Cu-Doped $\text{Mn}_3\text{Si}_2\text{Te}_6$

4.1.1 15% Cu

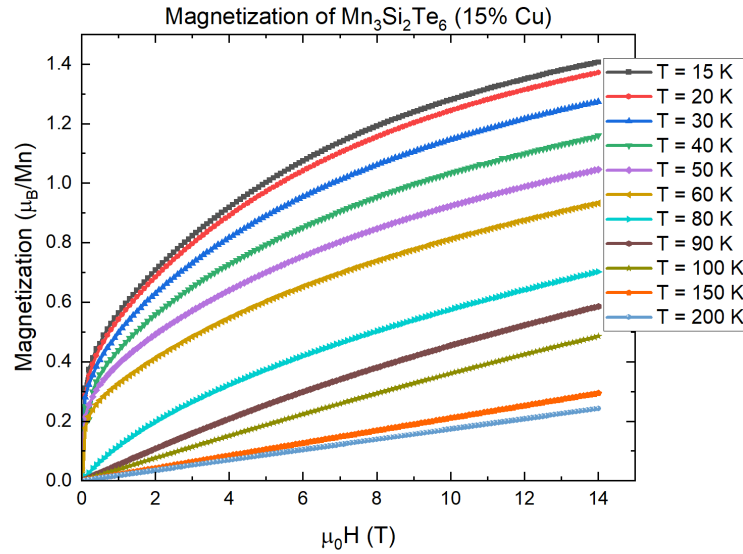


Figure 4.1: Magnetization vs. applied c-axis field at various temperatures for $\text{Mn}_3\text{Si}_2\text{Te}_6$ (15% Cu-Doped). Note that the units are listed as Bohr Magneton per Mn ion, but this calculation assumes all magnetization comes from the Mn while here Cu also contributes to magnetization, so this is not exact.

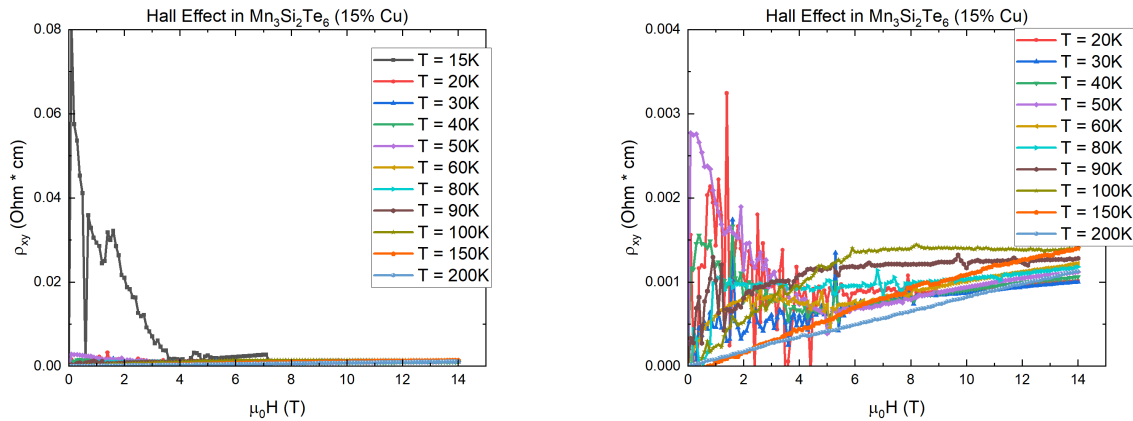


Figure 4.2: Left: The Hall Effect measured in $\text{Mn}_3\text{Si}_2\text{Te}_6$ (15% Cu-Doped). Hall data was also measured from -14T - 0T, and was largely the same with opposite sign. Right: A zoomed-in version excluding the 15K data so trends can be seen more easily.

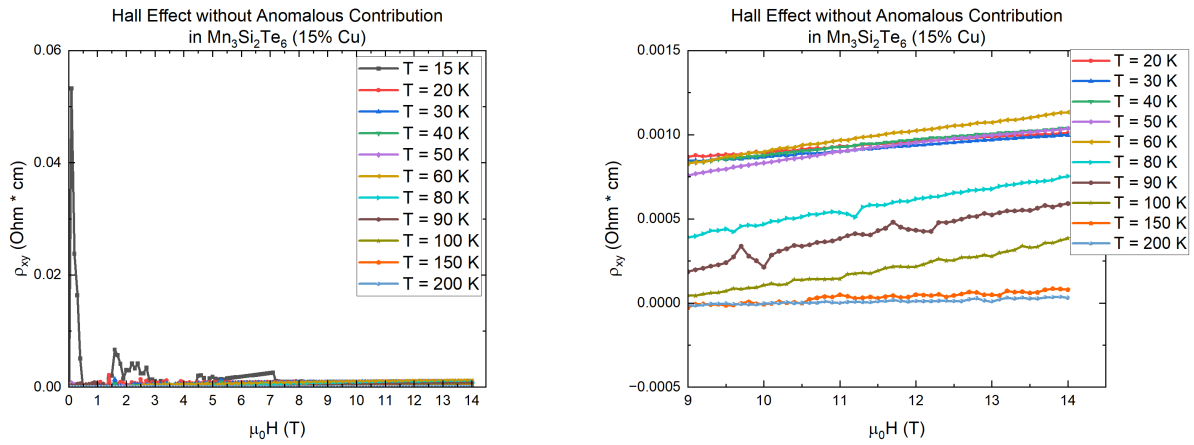


Figure 4.3: Left: The Hall Effect measured in $\text{Mn}_3\text{Si}_2\text{Te}_6$ (15% Cu-Doped) with the contribution from the AHE fitted for and subtracted, leaving approximately the linear ordinary contribution. Right: A zoomed-in version excluding the 15K data so trends can be seen more easily and focusing on the 9-14T range that was used for determining charge carrier density.

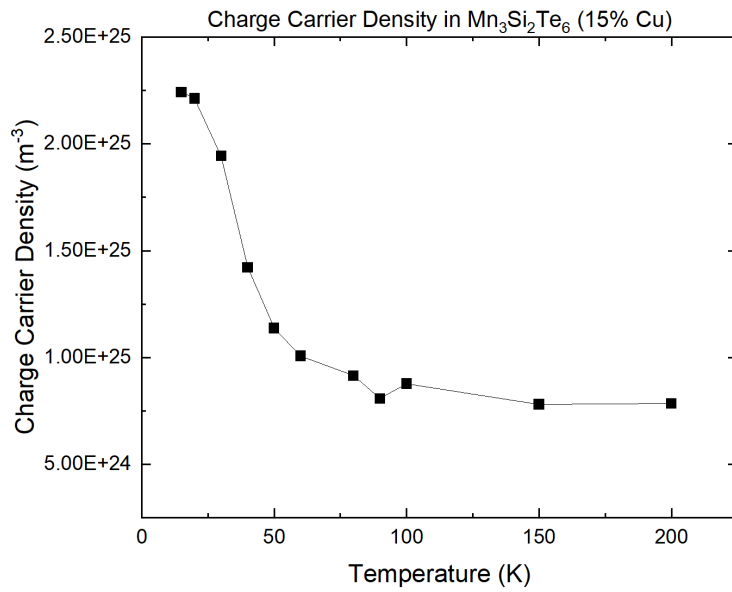


Figure 4.4: Charge carrier density at various temperatures for $\text{Mn}_3\text{Si}_2\text{Te}_6$ (15% Cu-Doped), determined from the Hall Coefficient.

4.1.2 30% Cu

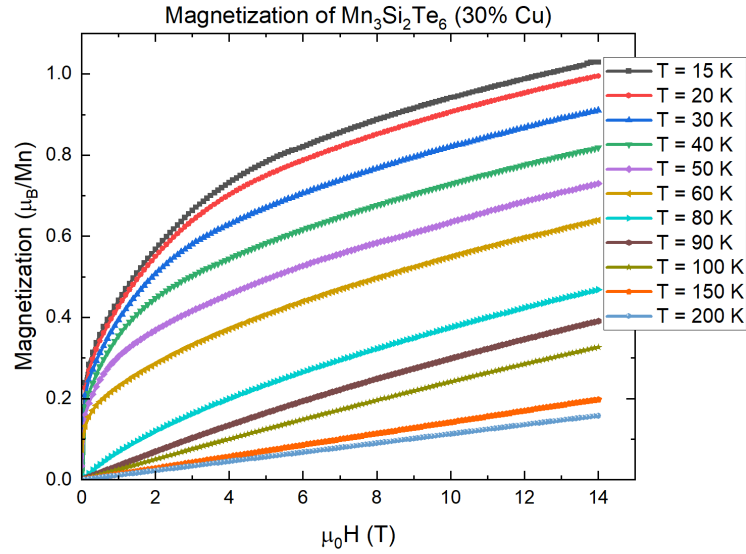


Figure 4.5: Magnetization vs. applied c-axis field at various temperatures for $\text{Mn}_3\text{Si}_2\text{Te}_6$ (15% Cu-Doped). Note that the units are listed as Bohr Magnetron per Mn ion, but this calculation assumes all magnetization comes from the Mn while here Cu also contributes to magnetization, so this is not exact.

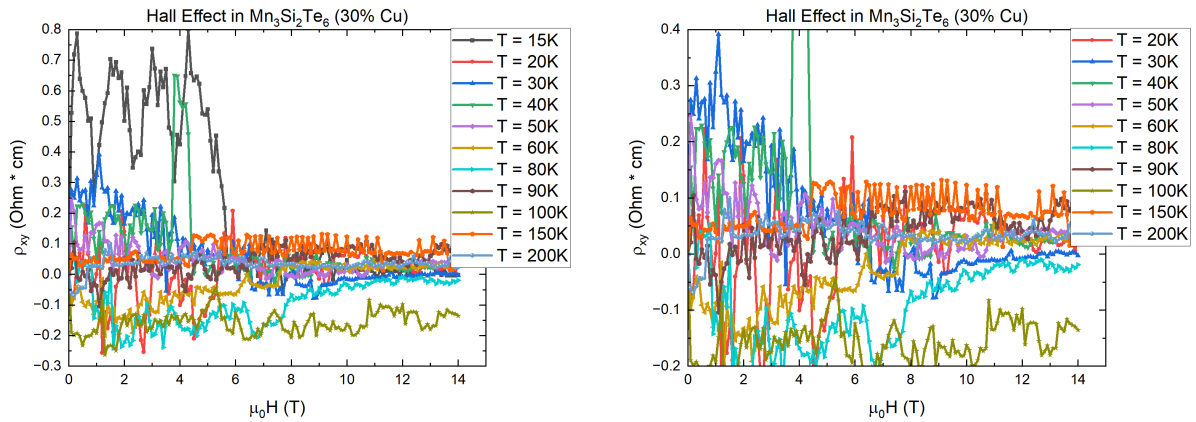


Figure 4.6: Left: The Hall Effect measured in $\text{Mn}_3\text{Si}_2\text{Te}_6$ (30% Cu-Doped). Hall data was also measured from -14T - 0T, and was largely the same with opposite sign. Right: A zoomed-in version excluding the 15K data so trends can be seen more easily.

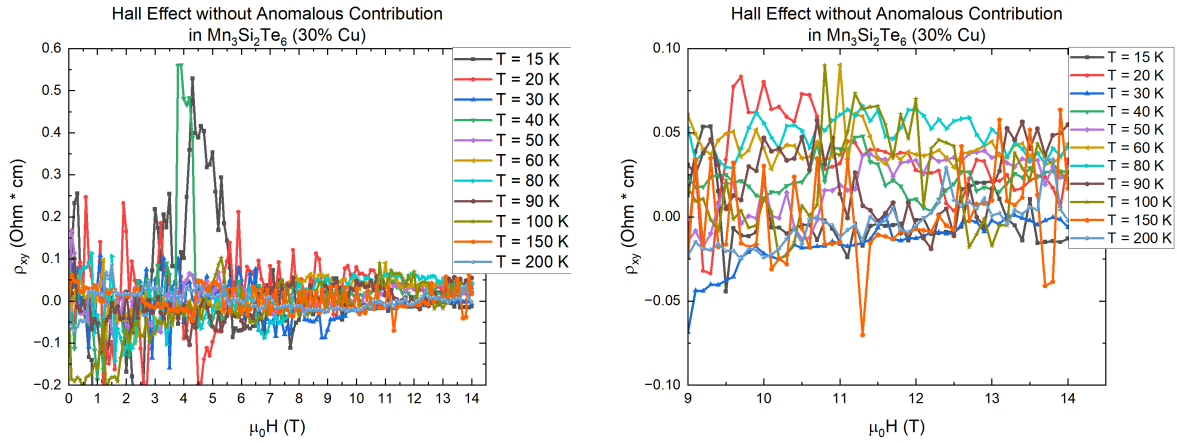


Figure 4.7: Left: The Hall Effect measured in Mn₃Si₂Te₆ (30% Cu-Doped) with the contribution from the AHE fitted for and subtracted, leaving approximately the linear ordinary contribution. Right: A zoomed-in version excluding the 15K data so trends can be seen more easily and focusing on the 9-14T range that was used for determining charge carrier density.

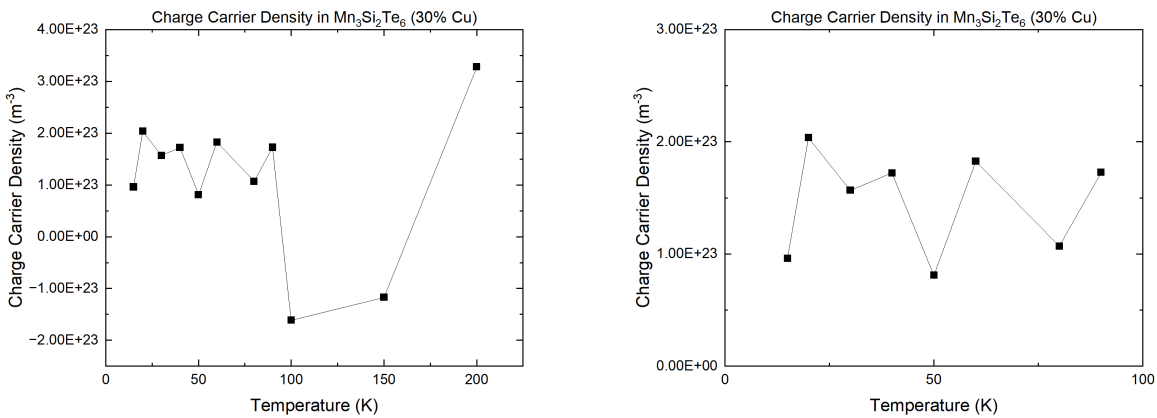


Figure 4.8: Left: Charge carrier density at various temperatures for Mn₃Si₂Te₆ (30% Cu-Doped), determined from the Hall Coefficient. The negative carrier density values imply at those temperatures the primary carrier density has switched from electrons to holes. Right: A zoomed-in version only showing density below 100K, which is purely positive.

4.2 In-Doped $\text{Mn}_3\text{Si}_2\text{Te}_6$

4.2.1 15% In

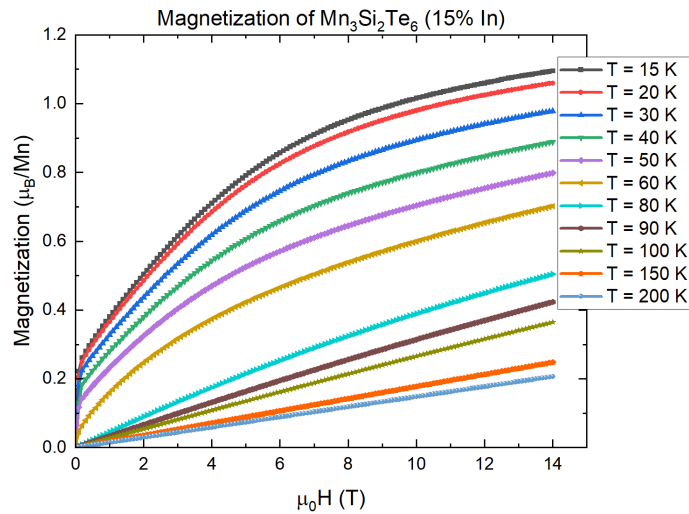


Figure 4.9: Magnetization vs. applied c-axis field at various temperatures for $\text{Mn}_3\text{Si}_2\text{Te}_6$ (15% In-Doped).

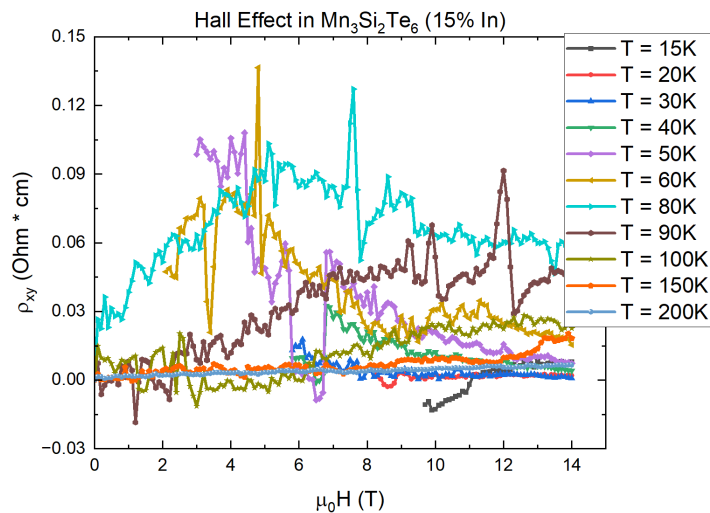


Figure 4.10: The Hall Effect measured in $\text{Mn}_3\text{Si}_2\text{Te}_6$ (15% In-Doped). Hall data was also measured from -14T - 0T, and was largely the same with opposite sign. Resistivities were unable to be measured for the full range at lower temperatures, so those datasets are truncated accordingly.

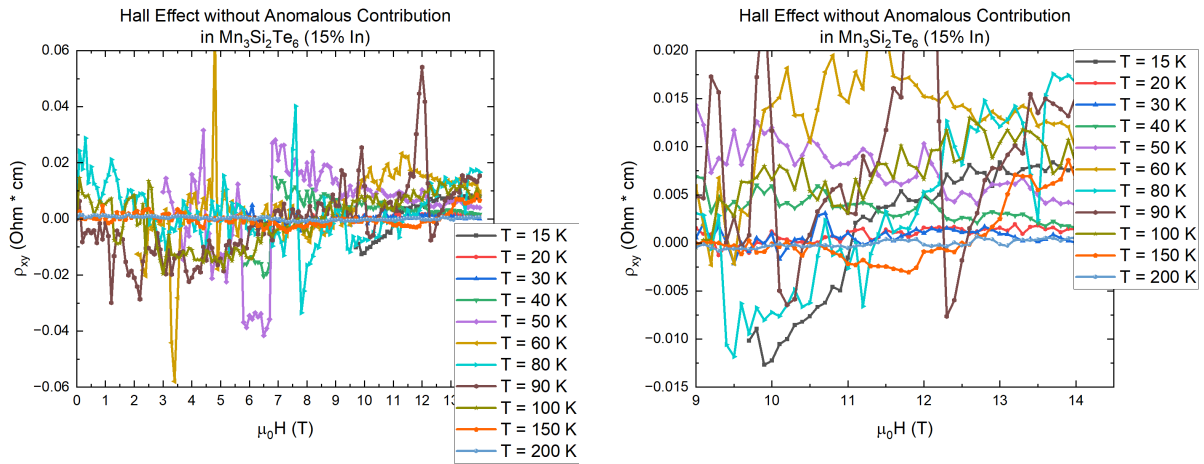


Figure 4.11: Left: The Hall Effect measured in Mn₃Si₂Te₆ (15% In-Doped) with the contribution from the AHE fitted for and subtracted, leaving approximately the linear ordinary contribution. Right: A zoomed-in version focusing on the 9-14T range that was used for determining charge carrier density.

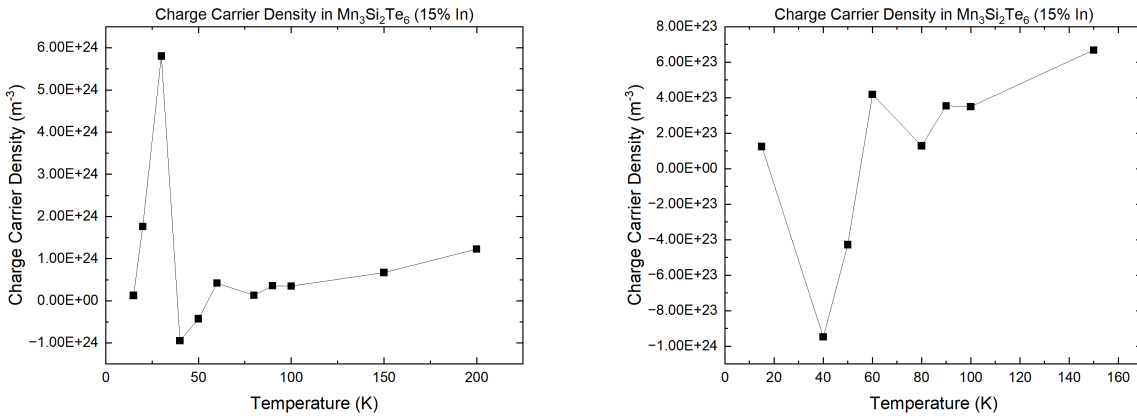


Figure 4.12: Left: Charge carrier density at various temperatures for Mn₃Si₂Te₆ (15% In-Doped), determined from the Hall Coefficient. The negative carrier density values imply at those temperatures the primary carrier density has switched from electrons to holes. Right: A zoomed-in version omitting the spikes at 20K, 30K, and 200K, so lower-density trending is easier to see.

4.2.2 30% In

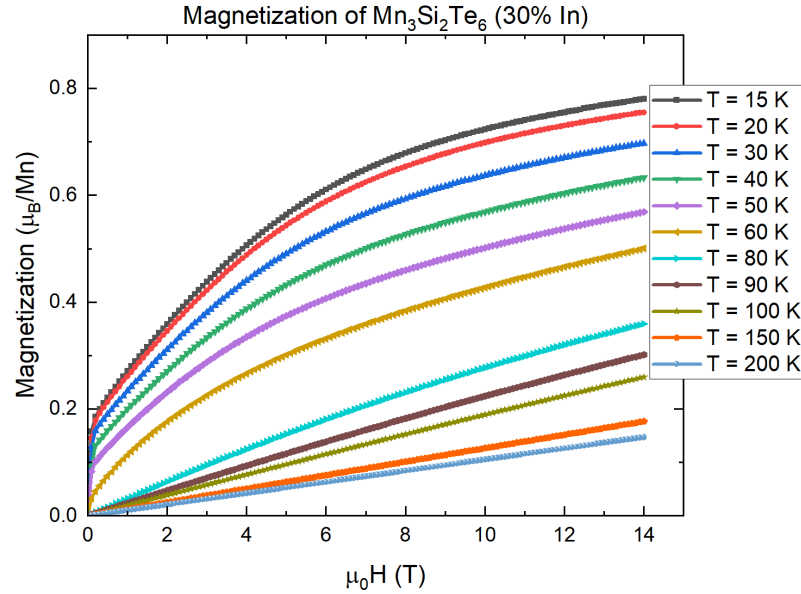


Figure 4.13: Magnetization vs. applied c-axis field at various temperatures for Mn₃Si₂Te₆ (30% In-Doped).

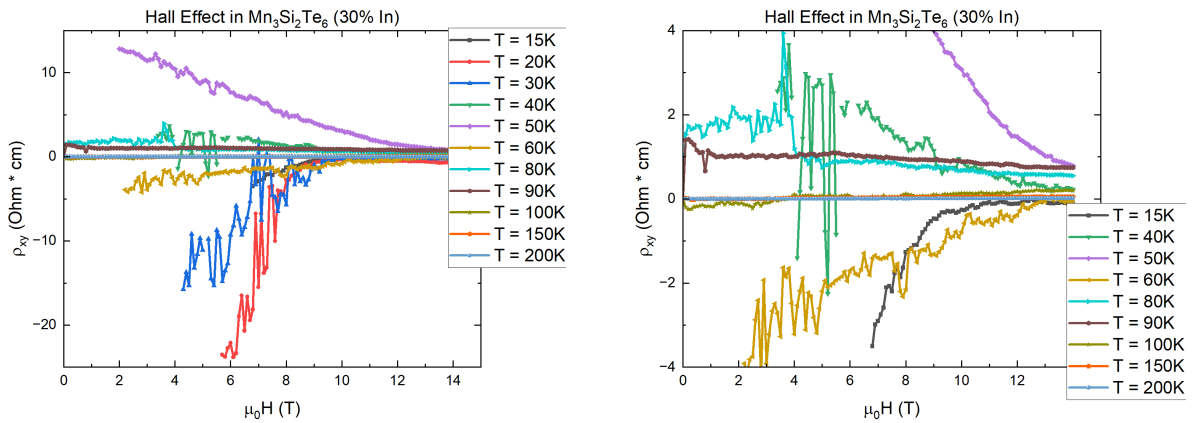


Figure 4.14: Left: The Hall Effect measured in Mn₃Si₂Te₆ (30% In-Doped). Hall data was also measured from -14T - 0T, and was largely the same with opposite sign. Resistivities were unable to be measured for the full range at lower temperatures, so those datasets are truncated accordingly.

Right: A zoomed-in version excluding the 20K and 30K data so trends can be seen more easily.

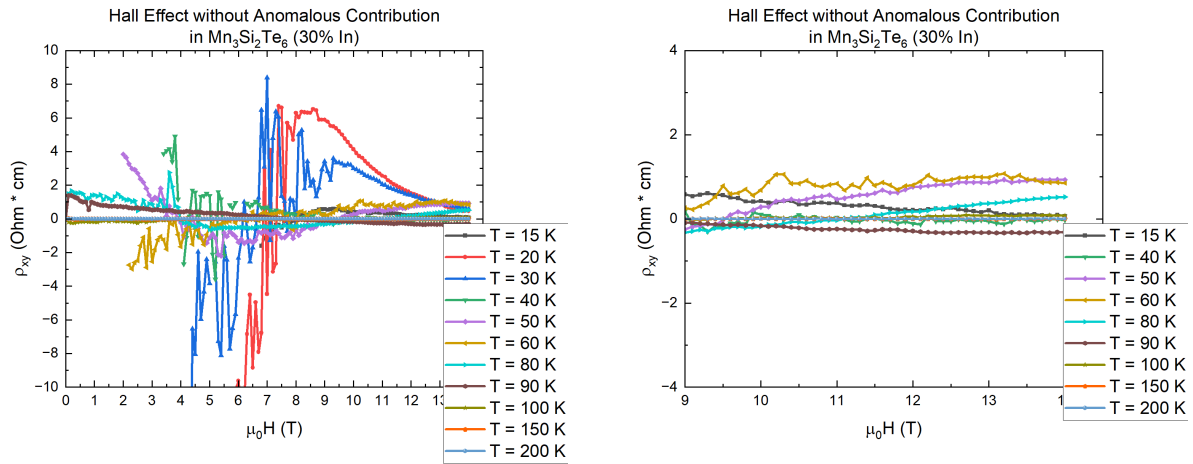


Figure 4.15: Left: The Hall Effect measured in $\text{Mn}_3\text{Si}_2\text{Te}_6$ (30% In-Doped) with the contribution from the AHE fitted for and subtracted, leaving approximately the linear ordinary contribution. Right: A zoomed-in version excluding the 20K and 30K data so trends can be seen more easily and focusing on the 9-14T range that was used for determining charge carrier density.

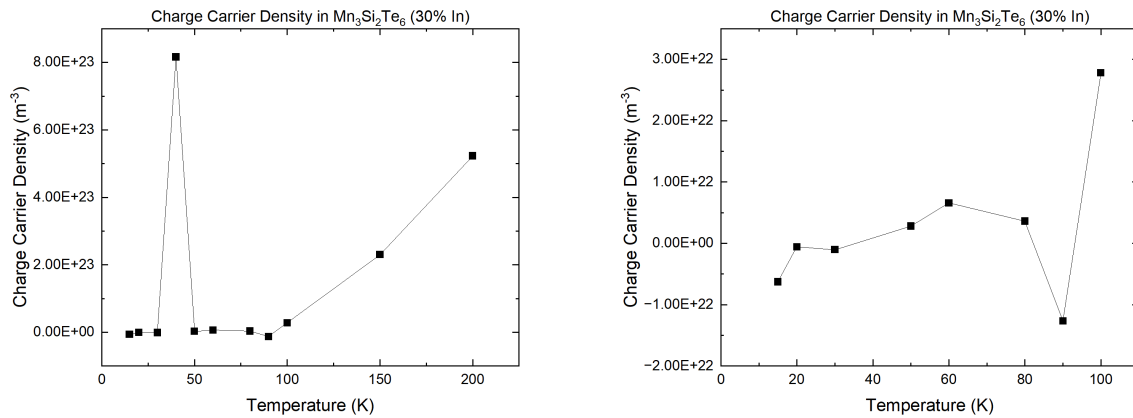


Figure 4.16: Left: Charge carrier density at various temperatures for $\text{Mn}_3\text{Si}_2\text{Te}_6$ (30% In-Doped), determined from the Hall Coefficient. The negative carrier density values imply at those temperatures the primary carrier density has switched from electrons to holes. Right: A zoomed-in version omitting the spike at 40K and higher values at 150-200K so lower-density trending is easier to see. Note the much lower magnitude than other sample carrier densities.

4.2.3 In-Doped Magnetization vs. Temperature

In addition to the results above collected by the author, the following Magnetization data was collected at 100 Oe (.01 T) by Dr. Yifei Ni. From this, phase transition temperatures were identified for the In-samples, which will be further discussed in Section 5. As shown on the graph below, for 15% In this temperature is around 56K, and for 30% In this temperature is around 44 K.

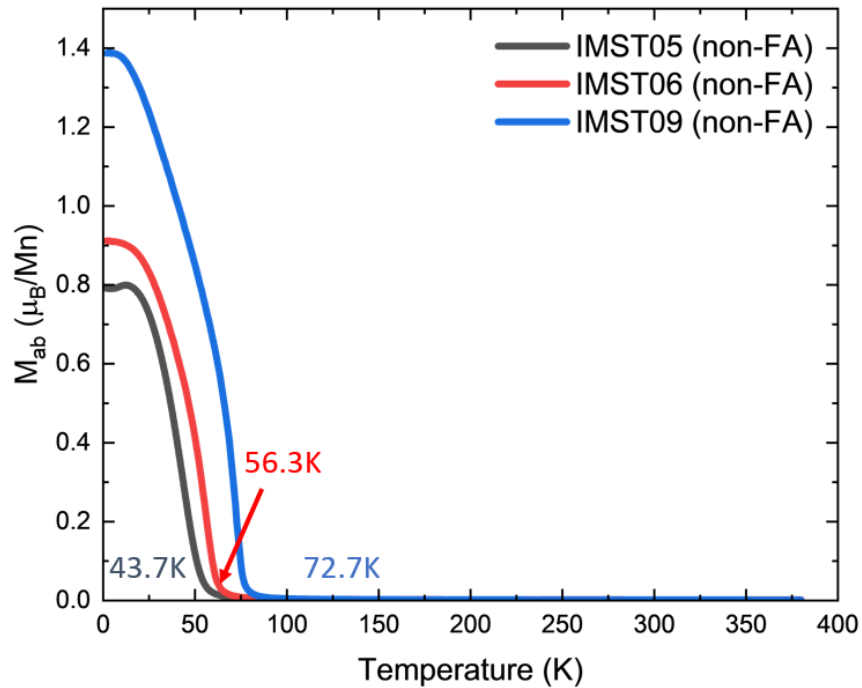


Figure 4.17: Magnetic moment vs. temperature for multiple In dopings of MST (IMST05 = 30%, IMST06 = 15%, IMST09 = 3%). The transition temperatures identified from this data are marked on the graph. (Credit for this work to Dr. Yifei Ni).

Chapter 5

Discussion

First, for comparison, it's important to look at the Hall Effect and computed charge carrier density in the original undoped MST [6]:

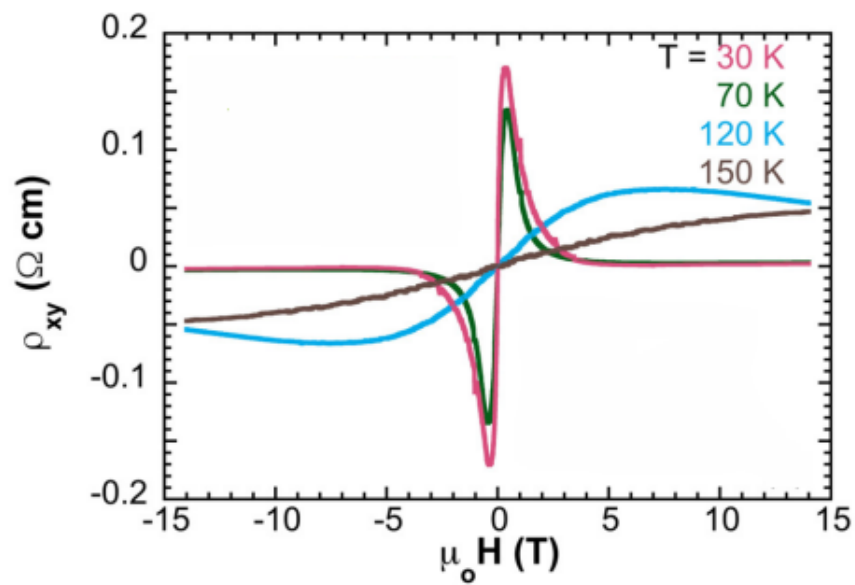


Figure 5.1: The Hall Effect measured in undoped $\text{Mn}_3\text{Si}_2\text{Te}_6$ [6].

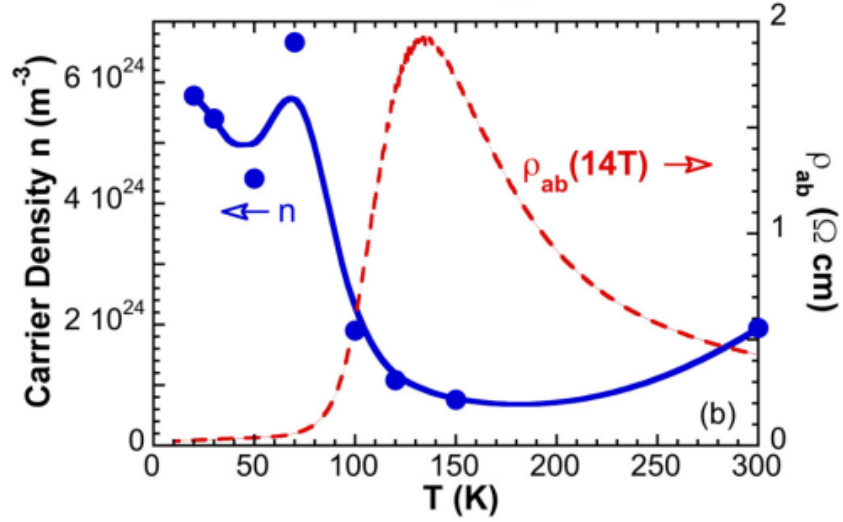


Figure 5.2: Charge carrier density at various temperatures for undoped $\text{Mn}_3\text{Si}_2\text{Te}_6$ [6], determined from the Hall Coefficient between 9-14 T [6].

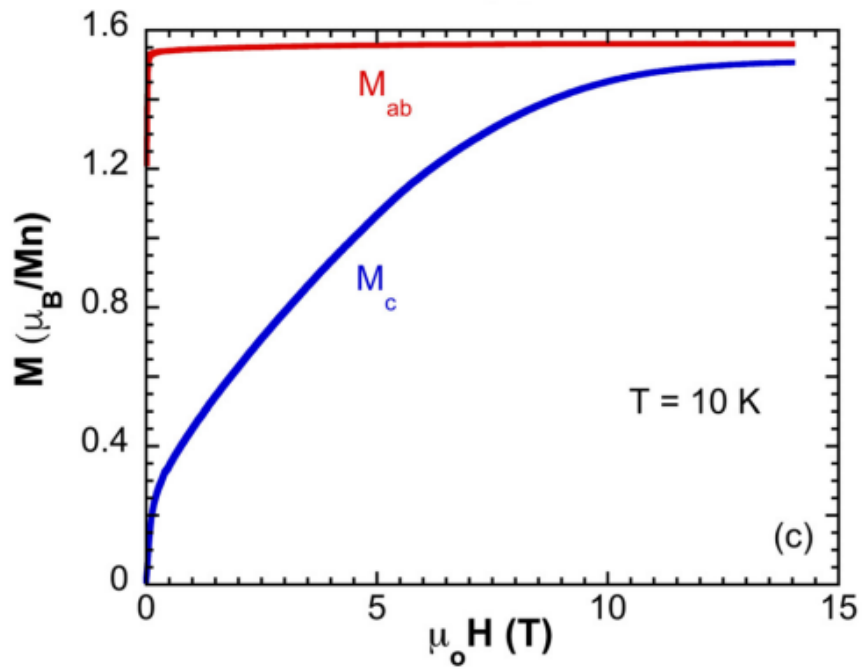


Figure 5.3: Magnetization along both the ab and c axes at 10 K for undoped $\text{Mn}_3\text{Si}_2\text{Te}_6$ [6]. Note that ab Magnetization saturates at a low field at a value of around 1.55 Bohr Magnetons per Mn ion, but c Magnetization increases more slowly and saturates at a lower value. This anisotropy is thought to be due to the magnetic moments of Chiral Orbital Currents (COC) subtracting from overall magnetization [5].

Comparing these datasets to the results presented in Section 4, it can be seen that the 15% Cu results are very similar to the undoped sample. Both display AHE at lower temperatures which dies out as temperature increases and linear Hall effect at high field, though for the Cu-doped the Hall resistivity is two orders of magnitude lower. The charge carrier densities also follow similar profiles, sloping sharply upwards below around 100 K, but the doping displays roughly double the carrier density. Taken together, these pieces of information suggest that a relatively small amount of Cu-ions dope well into the lattice and add additional free electrons, reducing normal resistivity without completely removing the magnetoresistance effects seen in pure MST.

Conversely, the 30% Cu doped results follow far less of a consistent trend. The Hall Effect behavior is more erratic at low field, though it does still become roughly linear with some spikes at higher field, and the charge carrier density lacks a clear trend. The dip to negative carriers (holes) between 100-150K is not necessarily unreasonable, as that has been reported in other measurements of pure MST [21].

The correlation between magnetization and carrier density is also noteworthy here. The 15% Cu doped sample displays largely similar c-axis magnetization to the undoped sample, both saturating around 1.4-1.5 Bohr Magnetons per magnetic ion. Conversely, the 30% Cu displays a magnetization saturating at around 1 Bohr Magnetons per magnetic ion, nearly 30% lower. This could indicate that the addition of too much Cu disrupts the structure in such a way as to substantially decrease magnetic moment and that in addition to the COC, the overall magnetization plays a role in electrical transport in the sample, explaining the substantially worse behavior in the 30% doping.

It's more difficult to compare Hall trends in the In-doped samples as a result of the resistivity data being incomplete, but it appears that 15% In similarly retains an AHE at low temperatures that dies out at lower field and more linear Hall response at high temperature. The trending is less consistent than with undoped and Cu-doped MST, but unlike the Cu-doped samples the order of magnitude matches between 15% In and undoped. At a glance the ordinary Hall appears to have less of a consistent linear trending than usual, but this could reflect a lower-quality fit due to the

original data, so further study is needed to confirm that claim. The charge carrier density is notable for being lower than undoped MST's already-low carrier density, though it briefly achieves a 10^{24} density at 30K. Combined with the sudden dip to negative carrier density (holes) as temperature declines from 60K to 40K, this could be suggestive of a transition in the material altering the properties, matching with the transition temperature of around 56K noted in the magnetization (See Figure 4.17).

Finally, the 30% In is difficult to characterise for the same reasons as 15%, but it's clearly visible that at lower temperatures the Hall resistivity displays substantial spikes from the AHE. Even at higher temperature and field, the magnitude of the resistivity is far larger than in any other samples measured. Matching this, the carrier density is far lower, remaining at order 10^{22} besides a spike at 40K. Again, this spike could be indicative of some transition in the material as temperature decreases, which would match the transition at 44K seen in the magnetization in Figure 4.17. In both cases, further study is likely required to confirm the presence and nature of such a transition.

As a last point of comparison, magnetization can again be examined, this time for the In dopings. In is not a magnetic ion so it would be expected for replacement of Mn with In to decrease magnetic moment, which is seen in both dopings [10]. Specifically, the magnetization of the 15% In is similar to 30% Cu, and the 30% In doping displays the lowest magnetization of any sample, never even reaching 1 Bohr Magneton per magnetic ion. Given the higher and more erratic Hall resistivities and lower charge carrier densities of the In dopings, this again implies magnetization has an effect on electrical transport in the crystal. Moreover, if the COC generated on MnTe structures were the only contributors to the observed CMR, and disrupting this MnTe structure was the only thing then causing higher resistivity, the 30% Cu and In dopings should have similar resistivities. As the 30% In is higher resistivity and displays notably lower magnetization, this further supports magnetization impacting electrical transport.

Overall, it appears that lower dopings (the 15% cases) imbue some of the properties of the dopant ion to MST without fully removing the behaviors of the base system. However, the larger 30% dopings display far more erratic behavior, lower magnetization, and higher resistance, so it's likely that dopings of this level and higher disrupt the structure to an unrecoverable degree. While there's not enough data to confirm, the results also support the idea that in addition to the presence of Chiral Orbital Currents on the MnTe structures, the net magnetization of the sample also affects the existence and degree of magnetoresistance.

Chapter 6

Conclusion

Through the course of this study, it was shown that Cu and In can be doped in for Mn in $\text{Mn}_3\text{Si}_2\text{Te}_6$, and 15% and 30% dopings were synthesized. The Hall Effect was measured in these doped samples to determine what effects the partial replacement of Mn has on MST's unique electrical transport properties. It was found that 15% dopings retain much of the behavior of base MST while adding additional effects based on the dopant ion. However, 30% dopings completely disrupt the electrical transport, leading to more erratic behavior. Overall it appears that MnTe structures specifically generate the Chiral Orbital Currents that cause/enhance CMR in the materials and substituting in other ions like Cu and In does not lead to the same behavior. However, COC don't appear to be the only items that affect electrical transport, as increased resistivity and decreased charge carrier density are also correlated with decreased net magnetization.

Moving forwards, this work and others on MST open several possibilities for additional study. As the In doping datasets weren't completed at all, they need to be repeated with equipment that can withstand higher voltages so the data can be fully fit and analyzed. For all datasets, measuring ab axis magnetization in addition to c axis would also be useful to roughly quantify the magnetic moment of the COC and confirm how much the presence of COC is reduced in various dopings. Recognizing that the lower percentage dopings preserve some of the original MST behavior, experiments with even lower dopings such as 5% and 10% should be attempted and the Hall Effect measured to determine at what point the benefits of additional ions can be achieved while maximizing the base sample's powerful CMR. Recent work on MST has also revealed the Hall Effect

in undoped MST displays a strong dependence on current below 5mA, so the Hall Effect should be measured in the dopings as well along a larger range of currents to see if this effect is retained in the doped samples [21]. Finally, it's possible that other ions may be able to be doped in for Mn, so this possibility ought to be investigated in the hopes that more unique behaviors or better control of the original CMR can be uncovered.

References

- [1] A. Pippard, *Magnetoresistance in Metals*. Cambridge University Press, 1989, ISBN: 978-0-521-32660-5.
- [2] W. Thomson, “On the electro-dynamic qualities of metals:—effects of magnetization on the electric conductivity of nickel and of iron,” *Proceedings of the Royal Society of London*, vol. 8, pp. 546–550, 1857.
- [3] T. N. Foundation, *The nobel prize in physics 2007*, <https://www.nobelprize.org/prizes/physics/2007/popular-information/>, [Online; accessed 10-March-2024], 2007.
- [4] A. P. Ramirez, “Colossal magnetoresistance,” *Journal of Physics: Condensed Matter*, vol. 9, pp. 8171–8199, 1997.
- [5] Y. Zhang *et al.*, “Control of chiral orbital currents in a colossal magnetoresistance material,” vol. 611, pp. 467–472, 2022.
- [6] Y. Ni, H. Zhao, and Y. Zhang, “Colossal magnetoresistance via avoiding fully polarized magnetization in the ferrimagnetic insulator $\text{Mn}_3\text{Si}_2\text{Te}_6$,” *Physical Review B*, vol. 103, 2021.
- [7] A. Zunger and O. I. Malayi, “Understanding doping of quantum materials,” *Chemical Reviews*, vol. 121, pp. 3031–3060, 2021.
- [8] E. F. Schubert, *Doping in III-V Semiconductors*. Cambridge University Press, 2005, pp. 241–243.
- [9] N. C. for Biotechnology Information, *Atomic radius in the periodic table of elements*, <https://pubchem.ncbi.nlm.nih.gov/ptable/atomic-radius/>, [Online; accessed 10-March-2024].
- [10] D. R. Lide, *CRC Handbook of Chemistry and Physics*. CRC Press, 2005, ch. Magnetic susceptibility of the elements and inorganic compounds.
- [11] E. Hall, “On a new action of the magnet on electric currents,” *American Journal of Mathematics*, vol. 2, pp. 287–292, 1879.

- [12] S. J. Ling, J. Sanny, and W. Moebs, *University Physics II - Thermodynamics, Electricity, and Magnetism*. Rice University, 2016.
- [13] S. H. Simon, *Solid State Basics*. Oxford University, 2012.
- [14] N. Nagaosa *et al.*, “Anomalous hall effect,” *Reviews of Modern Physics*, vol. 82, 2010.
- [15] *Instruction manual for model tm3030plus tabletop microscope*, Hitachi High-Technologies Corporation, 2016.
- [16] *Aztec user manual*, Oxford Instruments, 2013.
- [17] *Physical property measurement system dynacool user’s manual*, Quantum Design, 2014.
- [18] *Electrical transport option (eto) user’s manual*, Quantum Design, 2013.
- [19] T. R. Kuphaldt, *Lessons in Electric Circuits: Volume I - DC*. 2006.
- [20] *Vibrating sample magnetometer (vsm) option user’s manual*, Quantum Design, 2011.
- [21] Y. Zhang *et al.*, “Current-sensitive hall effect in a chiral-orbital-current state,” *arXiv preprint arXiv:2309.06610*, 2023.